Self-regulating soliton domain walls in microresonators

Heming Wang[1,†], Boqiang Shen[1,†], Lue Wu[1], Chengying Bao[1], Warren Jin[2], Lin Chang[2], Mark A. Leal[2], Avi Feshali[3], Mario Paniccia[3], John E. Bowers[2,*], and Kerry Vahala[1,*]
[1]T. J. Watson Laboratory of Applied Physics, California Institute of Technology, Pasadena, CA 91125, USA.
[2]ECE Department, University of California Santa Barbara, Santa Barbara, CA 93106, USA
[3]Anello Photonics, Santa Clara, CA
* jbowers@ucsb.edu, vahala@caltech.edu

Dissipative soliton Kerr frequency combs in microresonators have recently been demonstrated with self-injection locking. They have the advantage of turnkey deterministic comb generation, and also simplify dark soliton generation in the normal dispersion regime. Here, the formation process of dark solitons triggered by self-injection locking is studied by regarding them as a pair of domain walls that connect domains having different intracavity powers. The self-injection locking mechanism allows the domain walls to self-regulate position so that a wide range of dark soliton states can be accessed. Moreover, soliton duty cycle is readily controlled by the feedback phase. Direct imaging of the dark soliton pulse shape using the electro-optic sampling technique is used to verify the theory. The results provide new physical insights as well as a new operational modality for this important class of nonlinear waves.

Soliton microcombs [1] offer a path towards miniaturization of optical frequency comb technologies [2] onto photonic chips. And their integration with III-V pump lasers without the need for optical isolation [3–6] is an important step towards fully integrated chip-based soliton microcombs. The self-injection locking process [7], which was originally used to reduce laser linewidth [8–10] has been shown to create a new "turnkey" operating point [5] that eliminates complex startup and feedback protocols. This combination of features enables single-chip soliton microcomb devices that comprise heterogeneously integrated III-V pump lasers with microresonators [11]. Moreoever, the self-injection-locked "turnkey" operation simplifies access to dark soliton states [6]. Specifically, dark solitons exist under conditions of normal group velocity dispersion (GVD) [12–16] and their formation requires special spectral-design considerations (e.g., mode-crossing induced anomalous dispersion [13]). And self-injection locking makes it possible to turnkey-trigger dark solitons without these requirements [6]. However, despite this benefit, a theory describing the dark soliton microcomb generation process under conditions of self injection locking has not yet been established.

Here we analyze the formation process of such dark solitons in the self-injection locking regime. It is shown that nonlinear injection locking not only eliminates the startup protocols from a technical viewpoint [5, 6], but also provides a new physical understanding of these solitons, wherein two oppositely-oriented domain walls are able to regulate their own dynamics. Moreover, the set point in this self-regulation is controlled by the feeedback phase so that soliton duty cycle can be readily adjusted to vary comb spectra and optimize comb pump power efficiency. The concept of a domain wall was developed to describe a sheet-like boundary between spatial regions in which a discrete symmetry is broken [17, 18]. In optics, polarization domain walls and novel types of vector dark domain wall solitons have been theoretically predicted [19] and observed in a fiber ring laser [20, 21]. In the context of microresonators, the domain walls are the spatial counterpart of switching waves [22, 23]. Their dynamics are governed by energy balance and can be described by the Maxwell point, which plays a central role in soliton formation and self-injection feedback. A model is developed and validated by taking "snap-shots" of dark soliton shapes via the electro-optic sampling technique [24–26].

We consider a self-injection system consisting of a nonlinear ring-type resonator and a laser as shown in Fig.1a. The laser and resonator are directly coupled without optical isolation, allowing the backscattered light from the resonator to be fed back to the laser and alter its dynamics. Within the approximation of weak backscattering and fast laser dynamics, the intracavity field follows the same dynamics as in a conventional nonlinear resonator, described by the Lugiato-Lefever equation (LLE) [27] (see Supplementary Information):

$$\frac{\partial\psi}{\partial\tau} = -(1+i\alpha)\psi - i\frac{\beta_2}{2}\frac{\partial^2\psi}{\partial\theta^2} + i|\psi|^2\psi + f \qquad (1)$$

where ψ is the normalized intracavity field amplitude, τ is the normalized slow time, α is the normalized detuning (cold resonance frequency minus pump laser frequency) β_2 is the normalized group velocity dispersion (GVD), θ is the resonator angular coordinate (from 0 to 2π), and f is the normalized pumping term. The injection locking dynamics can be summarized through a locking equilibrium equation (see Supplementary Information):

$$\mathrm{Im}\left[\frac{e^{i\phi}}{1+i\alpha-2iP}\frac{\rho}{f}\right] = 0 \qquad (2)$$

Here ϕ is the feedback phase including contributions from the feedback path, backscattering and laser amplitude-phase coupling; P is the normalized intracavity power and ρ is the normalized average field. The overall locking dynamics can be understood to result from the simultaneous solution of two separate equations giving

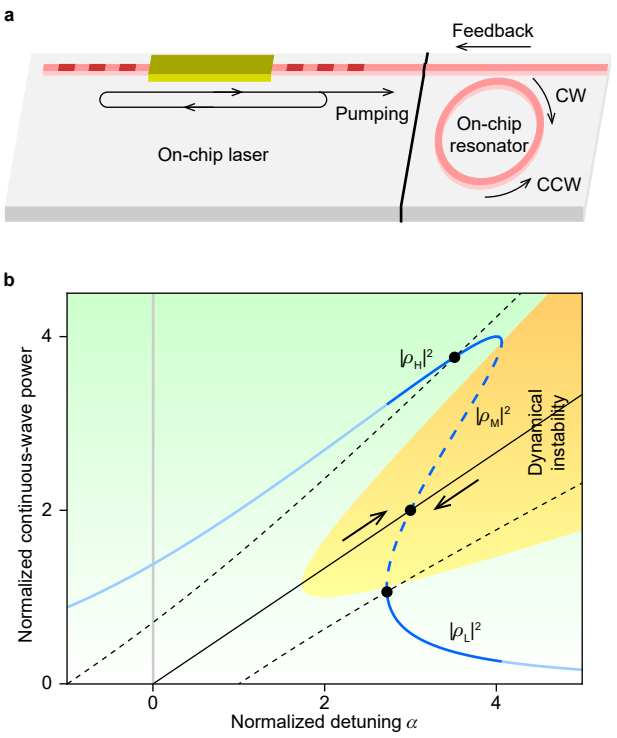

FIG. 1: **Laser-resonator system with nonlinear injection locking.** (a) Schematic of the system, where an on-chip laser is coupled to an on-chip microresonator without optical isolation, thereby allowing signals from the resonator to be fed back to the laser. Within the resonator, there are light circulating in both the clockwise (CW) and counter-clockwise (CCW) directions. (b) Blue curve shows the nonlinear resonator pumping curve for $|f|^2 = 4$, and the dashed blue line marks the instability section, which forms the orange region (marked with "Dynamical instability") when the pump power varies. The highlighted section shows the three branches of the multivalued part of the curve, and the powers correspond to $|\rho_{\mathrm{H}}|^2$, $|\rho_{\mathrm{M}}|^2$ and $|\rho_{\mathrm{L}}|^2$. Black lines show the laser locking curve in the presence of injection locking. The feedback phases are taken as $-\pi/2$, 0 and $\pi/2$ (from left to right). The black dots mark continuous-wave operating points of the system associated with these phases. The $\phi = 0$ curve is solid (others are dashed) and arrows show the evolution direction of the system.

first, the continuous-wave dependence of the intracavity power on detuning (herein called the resonator pumping curve), and second, the impact of feedback on the pump laser frequency (herein called the laser locking curve). These two equations are co-plotted in Fig.1b as the blue curve and solid black line. Their solution provides a new continuous-wave operating point in the resonator [5]. However, as now shown, because the operating point can lie within the dynamical unstable region, it provides a new mechanism of dark soliton formation and self regulation.

We first study a special case of zero second-order dispersion (i.e., $\beta_2 = 0$). Higher-order dispersion becomes important in the absence of β_2, but is also assumed zero in the model for simplicity, and does not qualitatively affect the results. Zero dispersion removes the field derivative terms from the LLE, which allows step discontinuities in the field. We proceed to show that such non-continuous-wave solutions exist and are stable in the absence of dispersion. This is related to the dynamical instability of the intracavity power. Referring to Fig.1b, the resonator pumping curve may have three branches with respect to the detuning α, and the field solutions are denoted as ρ_{H}, ρ_{M} and ρ_{L}, ordered by their absolute value from highest to lowest. Solutions on the upper (ρ_{H}) and lower (ρ_{L}) branches are readily shown to be stable while the middle branch solution (ρ_{M}) is unstable. The dynamical instability region indicated in Fig.1b can be determined from the LLE and plays a central role for comb generation.

In Fig.1b the continuous-wave operating point (Eq. 2) is visualized as the intersection of the resonator pumping curve and laser locking curves, and the power dependency of the laser locking curve may position the operating point on the middle unstable branch of the resonator pumping curve rather than the stable branches. As an example, the case of $\phi = 0$ can be shown to give $|\rho|^2 = 2\alpha/3$. This simple equation can be understood to result from self-phase modulation of the clockwise mode (Fig.1a) on itself (shifted by $|\rho|^2$) and cross-phase modulation of the clockwise mode on the counter-clockwise mode (shifted by $2|\rho|^2$). When pumping an initially unpumped resonator, the system is quickly pulled to the continuous-wave operating point, after which it evolves towards an operating point along the laser locking curve [5]. Overall, the system is driven to the effectively red-detuned region, where dynamical instabilities exist.

Since the operating point lies within the modulation instability regime, fluctuations cause the field to destabilize away from the operating point. Fields in about half of the resonator will increase to the upper equilibrium while fields in the other parts decrease to the lower equilibrium. However, these local changes must still satisfy the laser locking condition. This occurs in a spatially averaged sense wherein the average intracavity field and power determines the operating point. The whole process is illustrated in Fig.2a and 2b. As an aside, the average field will change in response to the power changes, but such changes cannot flip the upper equilibrium to the lower equilibrium or vice versa, as such a spontaneous flipping of the field requires large fluctuations that are exponentially unlikely.

In summary, beginning from the unstable branch operating point, the waveform evolves to become square-wave-like consisting of sections of upper and lower equilibria. We will refer to these sections as high-field and low-field domains, respectively (Fig.2b). Between these domains, a field discontinuity occurs. Such discontinuities are known as domain walls (Fig.2b), analogous to the domain walls that separate magnetic domains in ferromagnetic materials. A similar optical concept, known

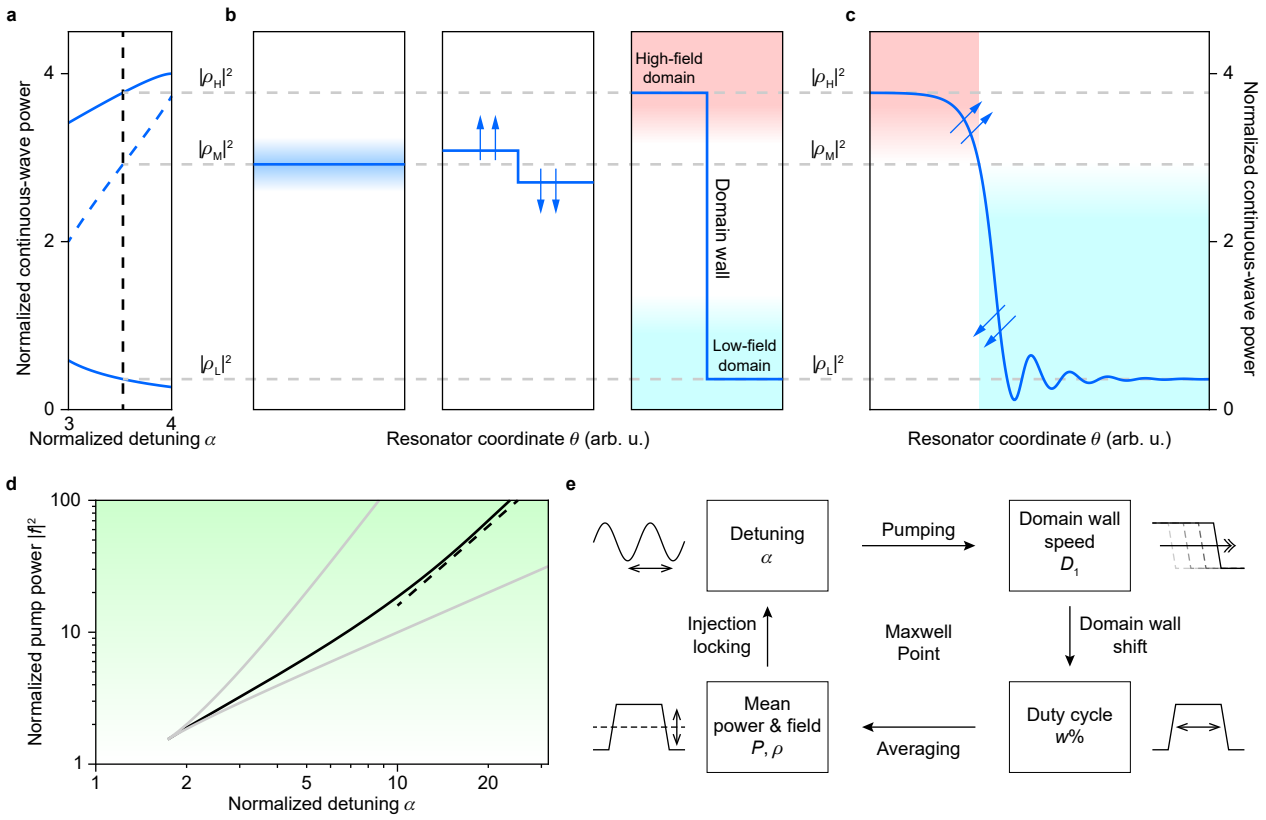

FIG. 2: **Formation dynamics of the dark soliton.** (a) A section of Fig.1b showing the three equilibria at a specific detuning $\alpha = 3.528$. (b) Evolution of the intracavity field in the absence of dispersion. Left panel: The intracavity field reaches ρ_M at the continuous-wave operating point, and there are fluctuations of the field (shown as blue shading and greatly exaggerated). Middle panel: The field evolves toward the upper and lower equilibrium. Arrows show the evolution direction of the respective fields. Right panel: high- and low-field domains appear in the resonator, and a domain wall forms to connect the two domains. (c) The domain wall solution for $|f|^2 = 4$ and finite normal dispersion. The red and blue areas mark the high-field and low-field domains, respectively. Arrows show the evolution direction of the respective field domains. (d) The Maxwell point (black solid curve) as a function of detuning. Gray curves are the boundaries for soliton generation. Black dashed curve is the α^2 estimate based on variational methods. (e) Block diagram illustrating the dark soliton self-regulation process in the self-injection locking regime.

as switching waves, has been extensively studied in fiber loops and resonators [22, 23, 28], but the name "domain wall" is used here to stress its spatial, rather than temporal structure, and to also note its topological origin as an object that continuously connects the high- and low-field domains. For the special dispersionless case initially studied here, the domain walls have zero width due to absence of the derivative terms in the LLE. The width becomes finite for the normal GVD regimes as discussed below.

For the normal dispersion case where $\beta_2 > 0$, the domain formation process is qualitatively similar to the dispersionless case. The system still reaches the continuous-wave operating point followed by the emergence of high- and low-field domains. However, the walls at the boundary of the domains are now finite width due to the dispersion term $\partial_\theta^2\psi$ which imposes a continuity condition on the field. The spatial width of the domain wall is assumed to be much shorter than 2π (cavity round trip) such that boundary effects can be ignored. This will be discussed later in terms of domain wall interactions.

Typical domain wall solutions to the LLE (normal dispersion) are plotted in Fig.2c. The domain wall can be roughly divided into two parts. The portion close to the high-field domain has the form of a constant term minus an exponential that increases to the upper equilibrium, while the portion close to the low-field domain is either exponentially or oscillatory decaying to the lower field equilibrium. These behaviors are controlled by the corresponding Lyapunov exponents at the equilibria. At the upper and lower equilibria, the energy gain of the field equals the energy loss. For the upper (lower) part of the domain wall, the optical gain (cavity loss) term is more prominent, and the field has the tendency to converge to ρ_H (ρ_L), expanding the high-field (low-field) domain. A stationary domain wall thus requires that these two

effects balance each other. Quantitatively,

$$\int \left(-2|\psi|^2 + 2\mathrm{Re}[f\psi^*]\right) d\theta = 0 \tag{3}$$

where the first term represents loss to the environment and the second term represents gain from the pump. If these tendencies are unbalanced, then the domain wall will move as a whole in the direction determined by the dominant tendency. The overall speed of the domain wall can be calculated from the energy imbalance (see Supplementary Information). With strong pumping, the domain wall converts pump energy to expand the high-field domain, while for weak pumping loss causes the high field domain to shrink. For steady state operations, a critical f value exist for a fixed detuning where the domain wall is in energy balance between pumping and loss. This value is known as the Maxwell point (MP) [23] denoted as f_{MP} and plotted in 2d. It can be determined by various analytical or variational methods. Near the critical point $\alpha = \sqrt{3}$, above which multiple equilibria can be found in the resonator, the MP can be obtained by asymptotic expansion, while for intermediate α values, MP can be estimated using variational methods based on the energy balance condition derived above (see Supplementary Information):

$$f_{\mathrm{MP}}^2 \approx \frac{\alpha^2}{2\pi} \tag{4}$$

Normally, it's challenging to tune a pumping laser exactly to the MP so as to stop the domain wall from moving. However, because the self-injection locking process relates α to the intracavity field, it provides a feedback loop necessary to maintain laser lock to the MP. For example, suppose that the intracavity field has split into a single low-field domain and a high-field domain under constant pumping. Therefore, two oppositely-oriented domain walls appear in the system. If the pumping field is stronger than f_{MP} at the initial detuning, the expansion of the high-field domain will increase both the average field norm and average power in the resonator, which, in turn, increases the detuning according to the nonlinear locking relation. This brings the detuning closer to the MP, and the movement of domain walls slow down. Eventually the detuning converges to the MP, and the domain walls stop moving where the combination of average field and power maintain the appropriate detuning. The opposite situation of an initial pump field that is too low case works in a similar way. To quantify the proportion of the high-field domain, we introduce the duty cycle variable, $w\%$, defined as the portion of the resonator with intracavity power higher than $|\rho_{\mathrm{M}}|^2$, which is analogous to the duty cycle describing square waves. The locking process is summarized in Fig.2e.

Domain walls are always generated in pairs with alternating orientations within a resonator subject to periodic boundary conditions on the field. If a pair of domain walls is close enough, then their exponential tails will overlap causing interactions between the domain walls. For the normal GVD case, domain walls attract each other when the high-field portions overlap, as the overlap integral leads to extra energy loss from the system (see Supplementary Information). This leads to collision and annihilation of the walls, and indicates that a bright-like pulse with $w\%$ close to 0% is unstable in a normal GVD system. The presence of extra energy input channels can stabilize such bright-like pulses (e.g., the pump mode eigenfrequency can be red-shifted compared to the parabolic dispersion [13, 15] such that pumping becomes more efficient). For domain walls with overlapping oscillatory tails near the low-field domain, the interaction will be alternating between attraction and repulsion depending on the relative position of the tails. This results in multiple equilibrium positions of the two walls, and has been studied previously using bifurcation theory [23]. These interactions unify the domain wall picture with conventional dark solitons as well as platicons generated with a fixed-detuning laser. If the pumping power is higher than f_{MP}^2, the two domain walls will move towards each other until their low-field portions overlap, at which point they start to interact and settle into equilibrium. If the pumping is too high, the maximum repulsion is not capable of holding the domain walls apart, leading to pair annihilation of the walls. This is consistent with the fact that dark solitons exist only within a very narrow region in the detuning-pump phase space [29]. From this point of view, the conventional dark solitons and platicons require the wall interactions to exist, which makes their duty cycles close to 100% and 0%, respectively. On the other hand, domain walls in the nonlinear self-injection-locked resonator can be independent of each other, since the detuning is instead determined by the duty cycle. And as a result, the duty cycle can reach an intermediate value close to 50%.

We now investigate the effects of the feedback phase, which will be shown to influence the soliton number (the number of dark pulses) as well as the duty cycle of dark solitons. As shown previously, dark solitons form from fluctuations on the unstable branch. Because these fluctuations are parametrically amplified by interaction with the pumping wave, the number of domain wall pairs generated in the resonator will be close to the relative mode number of the mode having the largest parametric gain (here relative mode number is defined as the actual mode number less the mode number of the pump mode). This in turn depends on the α and ρ coordinates of the operating point. Therefore the soliton number can be estimated given the operation point parameters (see Supplementary Information). We note that the exact soliton number is subject to domain wall collisions and other transient processes, and still has a certain degree of randomness. In some cases, single soliton operation is desirable due to its smooth spectrum and the lack of uncertainty of the distance between different solitons. This requires the gain to monotonically decrease with mode number relative to the pumping line, so that parametric oscil-

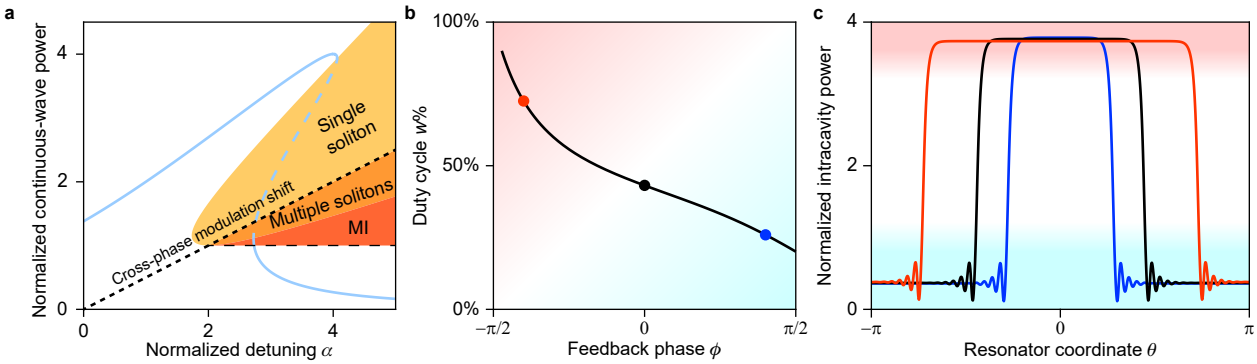

FIG. 3: **Control of soliton duty cycle using feedback phase.** (a) Phase diagram for the continuous-wave operating point showing regions corresponding to single and multiple soliton generation. The resonator pumping curve for $|f|^2 = 4$ is also shown. The conventional modulation instability region (MI) is also marked, where dark solitons can be generated but soliton number no longer depends on the mode number of the mode having the largest parametric gain. (b) Duty cycle of the generated dark soliton as a function of feedback phase for pump strength $|f|^2 = 4$, assuming the domain wall width is negligible compared to the resonator circumference. Smaller feedback phase relative to $\phi = 0$ leads to larger duty cycles, and vice versa. The colored dots correspond to panel (c). (c) Simulated soliton profiles for different feedback phases, with $\phi = -0.4\pi$ (red), $\phi = 0$ (black) and $\phi = 0.4\pi$ (blue), at pumping strength $|f|^2 = 4$.

lation occurs on the signal-idler pair that neighbor the pump. This can be shown to happen when the operating point is blue-detuned compared to the cross-phase modulation line $|\rho|^2 = \alpha/2$. For each pumping strength, this gives a specific range of the feedback phase (Fig.3a). We note that dark solitons can also emerge after the primary comb has formed inside the resonator through modulational instability (MI), in which case the soliton number no longer depends on the relative mode number for parametric gain, but on long-range fluctuations on top of the Turing roll pattern (see Supplementary Information).

Although the final detuning after soliton formation will be locked at the MP, the closeness between the MP and the initial continuous-wave detuning will determine the duty cycle that is needed to compensate for this difference. If the width of the domain wall is negligible compared to the scale of the resonator, ρ and P can be approximated as the weighted average of the high- and low-field domain contributions. The duty cycle can thus be related to the feedback phase via the locking condition (see Supplementary information) and $w\%$ can, in principle, be solved numerically (Fig.3b and c). Other quantities of interest, such as the overall comb power efficiency, can also be derived based on the duty cycle. We note that $w\%$ becomes independent of the soliton number within the approximation of thin domain walls.

We use the electro-optic sampling technique [26] to experimentally obtain waveforms of the dark solitons and to verify some of the above theoretical predictions. A commercial InGaAsP distributed-feedback (DFB) laser around 1556 nm is endfire coupled without optical isolation to an integrated silicon nitride/silica resonator (free spectral range 10.85 GHz) [6]. The field is collected from the drop port of the resonator to avoid the pumping field showing up in the result. The feedback phase is tuned by adjusting the gap between the laser and resonator. It is noted that implementation of a heater section beside the waveguide can enable the on-chip thermal control of feedback phase [11]. Soliton snapshots are obtained by mixing at a photodetector the dark soliton pulse train with an electro-optically (EO) generated comb having a slightly different repetition rate. The detailed experimental setup and data processing procedures can be found in the Methods. For different feedback phases, we are able to observe soliton states with different duty cycles (Fig.4a and b). The square-like waveform is apparent from the time evolution plot and its 3D representation. The variations of the field in both the high-field and low-field domains are believed to result from resonator inhomogeneity along the propagating direction as well as inaccuracies in the sampling process. As ρ_{M} cannot be accurately retrieved from the experiment, the pulse width here is determined instead as the portion with an optical power greater than the average of the 87.5% and 12.5% quantiles of the whole waveform. In strong contrast to previously demonstrated bright solitons, dark solitons or platicons, the measured pulse width occupies a significant portion of the resonator.

We have also swept the feedback phase by adjusting the coupling gap between the laser and resonator, and monitored the evolving field in the resonator during the scanning process (Fig.4c). When the feedback phase is decreasing, Turing rolls, breathing states and a single dark soliton can be observed during the single scan. Notably, the pulse width for a single soliton state near the end of the scan visibly widens. These observations are in good qualitative agreement with Fig.3a and 3b and consistent with MP predictions.

Noise spectra of the soliton repetition rate signal have also been measured, and a representative noise spectrum

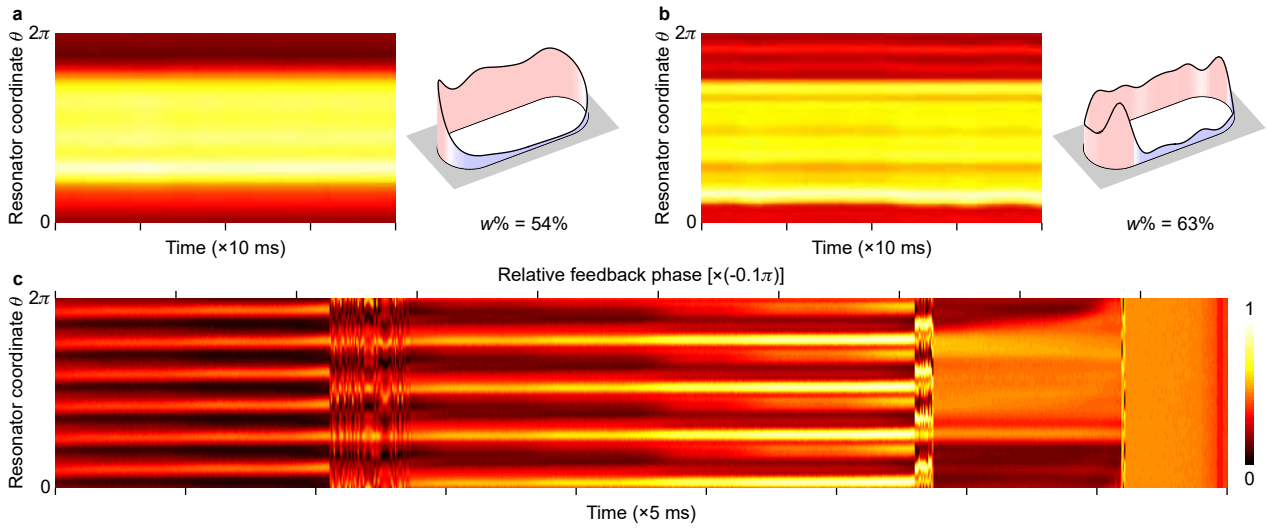

FIG. 4: **Measured dark soliton snapshots.** (a) Evolution plot for the intracavity field amplitude (false color) as a function of time and resonator coordinate with fixed feedback phase. Random drift of the soliton has been removed for clarity. Inset shows a 3D rendering of the averaged power profile on the racetrack resonator. The estimated duty cycle is also indicated. (b) Same as panel (a) but with a slightly different feedback phase. (c) Evolution plot for the intracavity field amplitude (false color) as a function of time and resonator coordinate measured while the feedback phase is decreasing. The estimated relative phase is derived from the applied piezoelectric voltage (see Methods).

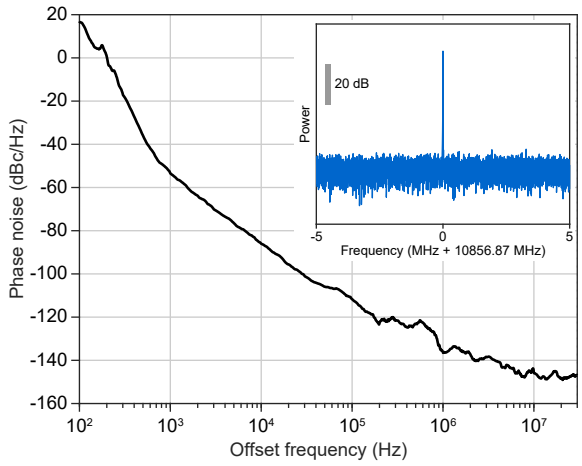

FIG. 5: **Representative phase noise spectrum of the dark soliton repetition rate signal.** Inset shows the measured repetition rate electrical spectrum with a resolution bandwidth of 1 kHz.

is shown in Fig.5. At 10 MHz offset frequencies, typical phase noise observed are −140 to −145 dBc Hz^{-1} and are comparable with previous bright [30] soliton systems with 10-GHz-scale repetition rates. We note that a 'quiet' operation point[31], where repetition rate noise is significantly depressed compared with normal operations, is also practical in the present systems.

There are many other effects that can be included in the model and these can lead to new phenomena in the system. For example, backscattering of the resonator β is heavily dependent on the geometry and fabrication details which can range from 10^{-3} to 10^{1}. Strong backscattering causes mode splitting and, when combined with optical nonlinearity, can lead to new modal dynamics. There have also been numerical efforts to generalize the backscattering to each pair of longitudinal modes [32], but the actual behavior of such scattering can be more complicated, with large amplitude and phase variations across different pairs of modes. High-order dispersion can also be added to the model. Similar domain-wall-like behavior of the pulse has also been shown in the numerical simulations [33] .

In summary, the formation dynamics of dark solitons in microresonators via the self-injection-locking process have been analyzed in terms of domain walls. And the resulting system has a new physical property associated with self regulation of the domain walls. The dark solitons were also imaged using an electro-optic sampling system, and the measurements verified predictions of the model. Self-regulation allows operation of the dark soliton microcomb at previously inaccessible duty cycles that offer high power efficiency comb states [16] as well as for microwave generation [6]. Duty cycle is controlled by the feedback phase, which in future designs could be electrically varied by way of, for example, an on-chip heater [11].

Acknowledgements.
The authors thank Q. Yang for discussions. Funding is provided by the Defense Advanced Research Projects Agency (DARPA) under A-PhI program (FA9453-19-C-0029) and the Air Force Office of Scientific Research (AFOSR) (FA9550-18-1-0353).

References

[1] Kippenberg, T. J., Gaeta, A. L., Lipson, M. & Gorodetsky, M. L. Dissipative Kerr solitons in optical microresonators. *Science* **361**, eaan8083 (2018).

[2] Diddams, S. A., Vahala, K. & Udem, T. Optical frequency combs: Coherently uniting the electromagnetic spectrum. *Science* **369**, eaay3676 (2020).

[3] Stern, B., Ji, X., Okawachi, Y., Gaeta, A. L. & Lipson, M. Battery-operated integrated frequency comb generator. *Nature* **562**, 401–405 (2018).

[4] Raja, A. S. *et al.* Electrically pumped photonic integrated soliton microcomb. *Nature Communications* **10**, 680 (2019).

[5] Shen, B. *et al.* Integrated turnkey soliton microcombs. *Nature* **582**, 365–369 (2020).

[6] Jin, W. *et al.* Hertz-linewidth semiconductor lasers using CMOS-ready ultra-high-Q microresonators. *Nature Photonics* (2021).

[7] Razavi, B. A study of injection locking and pulling in oscillators. *IEEE journal of solid-state circuits* **39**, 1415–1424 (2004).

[8] Liang, W. *et al.* Whispering-gallery-mode-resonator-based ultranarrow linewidth external-cavity semiconductor laser. *Optics Letters* **35**, 2822–2824 (2010).

[9] Liang, W. *et al.* High spectral purity Kerr frequency comb radio frequency photonic oscillator. *Nature Communications* **6**, 7957 (2015).

[10] Kondratiev, N. *et al.* Self-injection locking of a laser diode to a high-Q wgm microresonator. *Optics Express* **25**, 28167–28178 (2017).

[11] Xiang, C. *et al.* Laser soliton microcombs on silicon (2021). arXiv:2103.02725.

[12] Liang, W. *et al.* Generation of a coherent near-infrared kerr frequency comb in a monolithic microresonator with normal GVD. *Optics Letters* **39**, 2920–2923 (2014).

[13] Xue, X. *et al.* Mode-locked dark pulse Kerr combs in normal-dispersion microresonators. *Nature Photonics* **9**, 594–600 (2015).

[14] Huang, S.-W. *et al.* Mode-locked ultrashort pulse generation from on-chip normal dispersion microresonators. *Physical Review Letters* **114**, 053901 (2015).

[15] Lobanov, V., Lihachev, G., Kippenberg, T. & Gorodetsky, M. Frequency combs and platicons in optical microresonators with normal GVD. *Optics Express* **23**, 7713–7721 (2015).

[16] Xue, X., Wang, P.-H., Xuan, Y., Qi, M. & Weiner, A. M. Microresonator Kerr frequency combs with high conversion efficiency. *Laser & Photonics Reviews* **11**, 1600276 (2017).

[17] Zelâ€™Dovich, Y. B., Kobzarev, I. Y. & Okun, L. B. Cosmological consequences of a spontaneous breakdown of a discrete symmetry. *Sov. Phys.-JETP* **40** (1974).

[18] Weinberg, S. *The quantum theory of fields*, vol. 2 (Cambridge university press, 1995).

[19] Haelterman, M. & Sheppard, A. Polarization domain walls in diffractive or dispersive kerr media. *Optics Letters* **19**, 96–98 (1994).

[20] Zhang, H., Tang, D. Y., Zhao, L. & Wu, X. Observation of polarization domain wall solitons in weakly birefringent cavity fiber lasers. *Physical Review B* **80**, 052302 (2009).

[21] Zhang, H., Tang, D., Zhao, L. & Knize, R. Vector dark domain wall solitons in a fiber ring laser. *Optics express* **18**, 4428–4433 (2010).

[22] Rozanov, N. N., Semenov, V. E. & Khodova, G. Transverse structure of a field in nonlinear bistable interferometers. I. Switching waves and steady-state profiles. *Soviet Journal of Quantum Electronics* **12**, 193 (1982).

[23] Parra-Rivas, P., Gomila, D., Knobloch, E., Coen, S. & Gelens, L. Origin and stability of dark pulse Kerr combs in normal dispersion resonators. *Optics Letters* **41**, 2402–2405 (2016).

[24] Ferdous, F., Leaird, D. E., Huang, C.-B. & Weiner, A. Dual-comb electric-field cross-correlation technique for optical arbitrary waveform characterization. *Optics Letters* **34**, 3875–3877 (2009).

[25] Durán, V., Tainta, S. *et al.* Ultrafast electrooptic dual-comb interferometry. *Optics Express* **23**, 30557–30569 (2015).

[26] Yi, X., Yang, Q.-F., Yang, K. Y. & Vahala, K. Imaging soliton dynamics in optical microcavities. *Nature Communications* **9**, 3565 (2018).

[27] Lugiato, L. A. & Lefever, R. Spatial dissipative structures in passive optical systems. *Physical Review Letters* **58**, 2209–2211 (1987).

[28] Coen, S., Tlidi, M., Emplit, P. & Haelterman, M. Convection versus dispersion in optical bistability. *Physical Review Letters* **83**, 2328 (1999).

[29] Godey, C., Balakireva, I. V., Coillet, A. & Chembo, Y. K. Stability analysis of the spatiotemporal Lugiato-Lefever model for Kerr optical frequency combs in the anomalous and normal dispersion regimes. *Physical Review A* **89**, 063814 (2014).

[30] Yang, Q.-F. *et al.* Dispersive-wave induced noise limits in miniature soliton microwave sources. *Nature Communications* **12**, 1442 (2021).

[31] Yi, X. *et al.* Single-mode dispersive waves and soliton microcomb dynamics. *Nature Communications* **8**, 14869 (2017).

[32] Voloshin, A. S. *et al.* Dynamics of soliton self-injection locking in optical microresonators. *Nature Communications* **12**, 235 (2021).

[33] Anderson, M. H., Lihachev, G., Weng, W., Liu, J. & Kippenberg, T. J. Zero-dispersion kerr solitons in optical microresonators (2020). arXiv:2007.14507.

Methods

Experimental setup

The self injection locking dark soliton generation set up consists of the DFB laser chip enfire coupled to the integrated CMOS-ready ultra-high-Q microresonator chip. A fiber lens mounted on 3 independent precision translation stages is used to collect power from the microresonator chip waveguide. The optical waveguide facets and lens fiber port are aligned by fine tuning a micro-positioner. The laser stage is equipped with a piezoelectric control for all three translation degrees of freedom. For measurements with varied feedback phase, the gap between laser and resonator chip is tuned by applying a triangular signal to the piezoelectric controller of the laser stage. The transduction factor is measured as 0.42 μm V^{-1}, equivalent to about 1.1π feedback phase change per volt. Changing the gap also weakly affects the coupling efficiency between the laser and resonator, which is estimated to be < 0.5 dB for the tuning range used.

The EO comb used in the sampling measurement is generated using two phase modulators and one amplitude modulator followed by amplification using an erbium-doped fiber amplifier (EDFA). The sampling comb is then conditioned by a waveshaper to form the sampling pulse. The amplitude of each comb line is carefully trimmed and the comb has around 40 lines with equal intensity (variation < 1 dB). The dark soliton is collected via the fiber lens and mixed with the sampling comb on a photodetector (1 GHz bandwidth). The radio frequency signal is then collected by the oscilloscope, digitally demodulated and segmented. The segmentation length is variable and determined from the waveform to maintain the periodicity of the pulse and to correct for repetition rate drifting. Each piece of waveform is then down-sampled to 128 points for plotting and averaging.